Self-Limiting Evolution of Seeded Quantum Wires and Dots on Patterned Substrates

V. Dimastrodonato,[1] E. Pelucchi,[1] and D. D. Vvedensky[2]

[1]*Tyndall National Institute, University College Cork, Lee Maltings, Dyke Parade, Cork, Ireland*
[2]*The Blackett Laboratory, Imperial College London, London SW7 2AZ, United Kingdom*

(Received 29 February 2012; published 20 June 2012)

Extensive experimental data and an accompanying theoretical model are presented for the self-limiting profiles and Ga segregation on patterned GaAs(111)B substrates during metalorganic vapor-phase epitaxy of $Al_xGa_{1-x}As$. Self-limiting widths and segregation of Ga produce quantum dots along the base of pyramidal recesses bounded by (111)A planes and quantum wires along the vertical axis of the template, respectively. Coupled reaction-diffusion equations for precursor and adatom kinetics reproduce the measured concentration and temperature dependence of the self-limiting width and segregation. Our model can be extended to other patterned systems, providing a new paradigm for predicting the morphology of surface nanostructures and inferring their quantum optical properties.

DOI: 10.1103/PhysRevLett.108.256102 PACS numbers: 68.55.−a, 68.65.−k, 81.05.Ea, 81.10.Aj

The morphological evolution of a patterned crystalline surface driven by an incident flux of matter is among the most intriguing phenomena of surface physics. The main characteristics of growth morphologies on such substrates are due to different exposed facets having different kinetic and chemical properties. Processes such as the migration of precursors and adatoms, the dissociation of precursors, and the incorporation of adatoms each occur at facet-dependent rates. This results in a nonuniform growth rate across the substrate [1,2], with adjacent regions having different thicknesses and compositions which, for semiconductors, produces spatially-varying band gaps and, hence, carrier confinement [2]. Etched patterns can be used to channel mobile surface species to predetermined regions of a substrate, yielding uniform arrays of low-dimensional nanostructures [2–9].

The foregoing scenario is the basis for forming quantum wires (QWRs) at *V*-grooves [2,5] and quantum dots (QDs) at inverted pyramids [9] during metalorganic vapor-phase epitaxy (MOVPE) on etched GaAs substrates. These nanostructures are called "self-limiting" [10] because they result from the balance between the greater inherent growth rate of the side facets and capillarity, which favors growth on the bottom facet. Hence, the structural and compositional profiles of QWRs and QDs depend only on the bounding facets of the original pattern, the growth conditions, and alloy composition. This ensures reproducible lateral confinement and precise positioning, enabling the flexible and versatile design of optical nanosystems through the direct connection between geometry and excitonic spectra (see below).

Pyramidal QDs have wide-ranging properties and applications, including (i) the reproducible formation of excitonic states, which provides uniform single photon emission [11–13], (ii) precise coupling in quantum electrodynamic cavities [14] because of accurate site and energy control, and (iii) efficient emission of polarization-entangled photons [15] owing to the high-symmetry [111] growth orientation and the spatial uniformity provided by the patterned substrate. The dependence of the optical transition polarization on the QD shape, size, and symmetry [16] has recently been extended to an analysis that reveals the delicate interplay between the excitonic fine structure and the symmetry and composition of QDs [17]. Identifying the atomistic mechanisms responsible for the self-limiting profile would enable direct control over the geometry of the nanostructure. This would lead to reduced fine-structure effects, pave the way toward more reliable sources of entangled photons, and have an immediate and far-reaching impact on the field of quantum information.

Yet, despite the evident broad appeal of pyramidal QDs, their atomistic formation mechanisms are poorly understood. The systematic characterization of the self-limiting profile as a function of the growth conditions and composition, a key ingredient in model development, has not been readily available because of the painstaking procedures needed to acquire these data. On the other hand, previous work [18] has indicated that a reaction-diffusion model based on the surface diffusion and decomposition at step edges of the group-III precursor explains the morphology of misoriented GaAs(001) surfaces during MOVPE. In fact, the large length scales of typical etched patterns effectively preempt kinetic Monte Carlo simulations except for qualitative studies [19], leaving a continuum description as the only viable alternative for a quantitative theory.

We present here extensive experimental data and an accompanying theoretical model of self-limiting growth by MOVPE of AlGaAs QDs within tetrahedral recesses patterned on GaAs(111)B surfaces. Our study provides experimental evidence for the self-limiting profile as a function of both alloy content and growth temperature (T_G) and explains the experimental trends in terms of reaction-diffusion equations for the main steps of the

 © 2012 American Physical Society

growth process. Two sets of AlGaAs/GaAs samples were grown with the goal of reproducing (I) the modulation of the Al content of the ternary compound and (II) the variation of T_G (at a fixed alloy composition) [20]. All samples were structurally characterized by atomic force microscopy (AFM) with systematic profiling analyses, involving measurement and image processing routines and minimizing any geometrical and AFM tip artifacts [21]. Our results establish a new paradigm for the future development of seeded nanostructures based on the judicious combination of experimental measurements and theoretical modelling, which could play a pivotal role when a particular design is needed for specific requirements.

Figures 1(a) and 1(b) show AFM cross-sectional scans of two representative samples in batch I. Figure 1(a) tracks the evolution of the self-limiting profile for several Al compositions. An increase of Al content causes a narrowing of the base profile width along the vertical axis of the template (the dashed black lines, drawn only on the upper part of each layer, are a guide to the width narrowing). This effect is especially apparent when pure GaAs is grown on $Al_{0.55}Ga_{0.45}As$, where a sharpening of the profile is clearly evident [highlighted by the black dashed line in Fig. 1(b)]. Figure 1(c) shows how the self-limiting profile changes with T_G at constant Al content. A systematic analysis of the samples from batch II reveals that increasing T_G enhances the capillarity [23] from the sidewalls to the bottom, which increases the growth rate on the base and, therefore, broadens the basal profile.

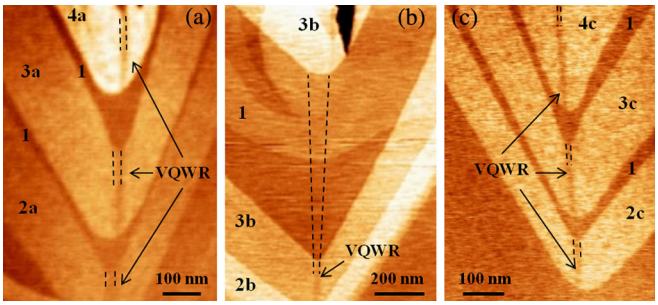

FIG. 1 (color online). Representative flattened [22] AFM cross-sectional scans of pyramidal systems consisting of pairs of $Al_xGa_{1-x}As$ (brighter) and GaAs markers (darker, indicated with 1), grown by varying the alloy composition [batch I, (a) and (b)] and the growth temperature [batch II, (c)]. (a) $x = 0.2$, 0.4, and 0.65 (layers 2a, 3a, and 4a, respectively) and (b) $x = 0.75$, 0.55, and 0 (layers 2b, 3b, and 1, respectively) to reproduce the modulation of the profile. (c) The widening of the $Al_{0.3}Ga_{0.7}As$ self-limited profile is reproduced by increasing the temperature from ~881 to 904 and then to 926 K (layer 4c, 3c, and 2c, respectively). Vertical QWRs (VQWRs) self form along the vertical axis of the structure during the deposition of AlGaAs due to Ga segregation. The cleavage plane intersects the vertex and midpoint of the opposite base of the triangular recess, resulting in different apparent thickness on the left and right sides of the central axis.

The self-limited width of the QDs in the inverted pyramids results from a combination of the geometry of the bounding facets, the kinetics on each facet, and interfacet surface diffusion. To reproduce the periodicity of the templates [Fig. 2(a)], we divide the substrate into identical unit cells, each consisting of a recess composed of a flat (111)B base and the lateral (111)A surfaces, as delivered by chemical etching after patterning [Fig. 2(b)]. Since, as we shall demonstrate, the self-limiting profile is due to the kinetics at the bottom of the recess, the top planar surface can be neglected, which effectively decouples the recesses from one another. To obtain an analytically tractable model, while retaining the essence of the pattern, we replace the pyramidal recess by an inverted truncated conical recess, as shown in Fig. 2(c). The (111)B base is a circle of diameter L_b^*, the length of the self-limiting profile, and the (111)A lateral facets, with length L_s, form the sides of the truncated cone.

We suppose that the precursors trimethylgallium (TMGa), trimethylaluminum (TMAl), and arsine (AsH_3) arrive at the substrate by diffusion through a boundary layer. Because of the arsenic-rich conditions, we consider the kinetics only of the group-III species and their precursors, as the concentration of arsenic is presumed not be rate limiting in any surface reaction [24]. Atoms are released by the decomposition of precursors at step edges, whereupon they diffuse until incorporated into the growth front. The adatom concentration n_i on each facet i is a solution of the stationary diffusion equation

$$D_i \nabla^2 n_i + F_i - \frac{n_i}{\tau_i} = 0, \tag{1}$$

in which D_i is the diffusion constant, F_i the effective atomic flux, and τ_i the lifetime to incorporation. There are separate equations for Ga and Al on each facet, so each quantity in this equation has a value for each atomic type [Fig. 2(d)]. We consider only stationary solutions, as our

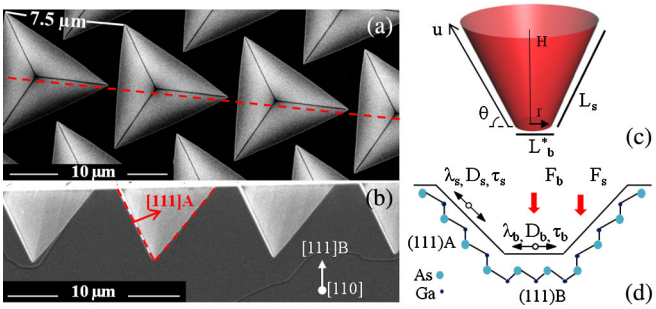

FIG. 2 (color online). Representative scanning electron micrographs in top (a) and cross-sectional (b) view of GaAs(111)B patterned with inverted tetrahedral pyramids with a pitch of 7.5 μm. The lateral facet edge is highlighted in red (dashed line) and its [111]A crystallographic orientation is indicated in (b). (c) Truncated conical model of a pyramidal recess. (d) Cross section of the recess along the (110) plane. The parameters $F_{s,b}$, $\lambda_{s,b}$, $D_{s,b}$, and $\tau_{s,b}$ are indicated on each facet.

interest is the self-limiting profile, rather than the evolution towards this profile.

In the first term in Eq. (1), the adatom diffusion coefficient D_i is given by the Arrhenius expression

$$D_i = a^2 \nu \exp\left(-\frac{E_i^D}{k_B T}\right), \tag{2}$$

where a is the jump length, taken as the nearest neighbour lattice spacing, $\nu \sim 10^{13}$ s^{-1} the attempt frequency, E_i^D the energy barrier to hopping, k_B is Boltzmann's constant, and T the absolute temperature [25].

The effective atomic fluxes in the second term in Eq. (1) are products of precursor fluxes and their facet-dependent [23,26] decomposition rates. The effective fluxes on the side and bottom regions, F_s and F_b, respectively, are linked by $F_s = rF_b$, where $r > 1$ accounts for the enhanced decomposition on the sidewalls. These fluxes are determined by requiring that the total deposition of group-III precursors corresponds to a growth rate of 1 monolayer (ML)/s and that the growth rate F across the unit cell is related to the growth rates of the individual facets by

$$A_b F_b + A_s F_s = (A_b + A_s)F, \tag{3}$$

where A_b and A_s are the areas of the base and side facets. For $Al_xGa_{1-x}As$ the total deposition flux of Al atoms is $F_i^{Al} = xF_i$ while, for Ga, $F_i^{Ga} = (1-x)F_i$, with F_i calculated from Eq. (3) for each species. Once $r^{Al,Ga}$ are fixed, the effective atomic deposition fluxes on each facet are determined by experimentally controllable parameters.

Finally, in the third term in Eq. (1), experimental observations, mainly from molecular-beam epitaxy [27], suggest an exponentially decreasing lifetime with temperature. Hence, for the ith facet we take

$$\frac{1}{\tau_i} = \nu_i \exp\left(-\frac{E_i^\tau}{k_B T}\right), \tag{4}$$

with frequency prefactor ν_i and energy barrier E_i^τ.

The concentrations of Ga and Al within the conical recess are determined from the general solutions of Eq. (1) for the bottom facet and the sidewalls. For the circular bottom facet, we express Eq. (1) in polar coordinates and obtain the (finite) solution

$$n_b(r) = F_b \tau_b + C_b I_0\left(\frac{r}{\lambda_b}\right), \tag{5}$$

with C_b an arbitrary constant, I_0 the modified Bessel function of the first kind of order zero, and $\lambda_b = (D_b \tau_b)^{1/2}$ the diffusion length on this facet.

The form of Eq. (1) on the conical side facets requires the Laplace-Beltrami operator on this curved surface [28]. The (finite) general solution of the resulting equation is

$$n_s(u) = F_s \tau_s + C_s K_0\left(\frac{L_b/2 + u\cot\theta}{\lambda_s \cos\theta}\right), \tag{6}$$

where u is the "radial" coordinate on the cone, θ the angle between the basal and side facets [Fig. 2(c)], C_s an arbitrary constant, K_0 the modified Bessel function of the second kind of order zero, and $\lambda_s = (D_s \tau_s)^{1/2}$ the diffusion length on this facet.

The arbitrary constants in Eqs. (5) and (6) are determined by requiring the adatom concentrations and currents to be equal at the facet boundary. This yields unique solutions for the concentrations from which the local growth rate, perpendicular to each facet, is calculated as

$$R_i(r) = \frac{dz_i}{dt} = \frac{\Omega_0}{\tau_i} n_i(r), \tag{7}$$

where $\Omega_0 = a^3$ is the atomic volume. The total growth rate is $R_i = R_i^{(AlAs)} + R_i^{(GaAs)}$. The self-limiting width L_b^* is obtained by requiring that the total growth rates at the boundary between side and bottom facets are equal:

$$\cos\theta [R_b^{(AlGaAs)}]|_{L_b = L_b^*} = [R_s^{(AlGaAs)}]|_{L_b = L_b^*}. \tag{8}$$

There are two types of parameters required for the solution of Eq. (8). Those in Table I are geometrical quantities and growth conditions, which are known from experiment. However, the kinetic parameters in Table II, which determine the rates of our surface processes, are difficult to measure directly in an MOVPE reactor and are not readily available from first-principles calculations. Accordingly, we will regard these as fitting parameters, but with restricted values. For example, our experimental observations, combined with studies of molecular-beam epitaxy [29], suggest faster diffusion of Ga on (111)A than on (111)B planes. The differences between atomic Ga and Al imply a shorter diffusion length and, therefore, a faster incorporation rate for Al. A shorter lifetime on the base facet gives a higher incorporation rate, which accounts for the capillarity-induced enhancement of the atom to be incorporated on that facet. Table II compiles the kinetic parameters for Al and Ga on each facet.

Figure 3(a) compares the experimental data collected from batch I and the calculated L_b^* as a function of alloy composition at $T_G = 938$ K. Apart from the quantitative agreement between experiments and theory, the qualitative trend confirms the experimental observation of a broad-

TABLE I. Experimental parameters used in Eq. (8) to determine the self-limited width in a conical recess [Fig. 2(c)]. a is the thickness of 1 ML, H the depth of the recess, θ the angle between the bottom and side facets, and T_G the growth temperature.

Parameter	Value
a	2.71×10^{-10} m
H	$22\,140a = 6 \times 10^{-6}$ m
θ	75°
T_G	870–938 K

TABLE II. Kinetic parameters used in Eq. (8) to determine the solution of the self-limited width.

Parameter	Al	Ga
E_b^D (eV)	2.10	1.70
E_s^D (eV)	1.40	1.00
E_b^τ (eV)	0.1511	0.0294
E_s^τ (eV)	0.1702	0.055
ν_b (s^{-1})	33.33	3.03
ν_s (s^{-1})	3.84	0.81
r^k	1.6	1.1

ening profile as the Ga concentration increases. Ga adatoms diffuse over longer distances than Al, so a higher Ga concentration can be expected to diffuse from the sidewalls toward the basal plane, whereupon the atoms can be promptly incorporated (the lifetime on the bottom being shorter than on the lateral facets). This leads to an increased growth rate on the bottom facet, which is accompanied by a widening of the self-limiting profile as shown in the inset of Fig. 3(a). More detailed analysis shows that the self-limited profile results not just from kinetics but also from a delicate balance between geometry and kinetics (see Supplemental Material [30] for details).

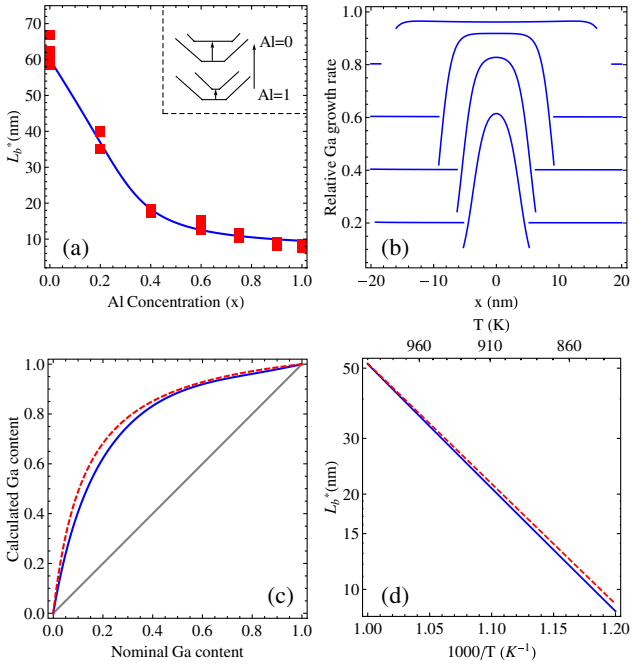

FIG. 3 (color online). (a) Experimental (red squares) and theoretical (blue curve) values of L_b^* as a function of Al content for the pyramidal template at $T_G = 938$ K. The blue curve was calculated from Eq. (8) with the parameters in Tables I and II. (b) Calculated steady-state Ga relative growth rates from Eq. (7) with the values of L_b^* obtained from Eq. (8). Nominal Ga content is 0.2, 0.4, 0.6, and 0.8 from bottom to top. The discontinuities are caused by differences between kinetic parameters on adjacent facets. (c) Comparison between calculated steady state (blue, solid trace) and fit to experimental values (red, dashed trace) from Ref. [32] of the Ga content in the middle of the pyramidal recesses as a function of the nominal alloy composition. The straight gray line represents the Ga concentration incorporated with no segregation. (d) Calculated L_b^* (blue, solid trace) and fit to experimental values (red, dashed trace). L_b^* is found by solving Eq. (8), fixing the Al content equal to 0.3 and varying T_G in the range 830–1000 K.

Figure 3(b) shows the spatial dependence of the Ga concentration profiles for different nominal Ga contents. As expected from experimental observations, our theory exhibits an enrichment of the relative Ga growth rate on the bottom facet, leading to an appreciably higher Ga concentration on the base than on the sidewalls where the Ga concentration is equal to the nominal value. However, as the nominal Ga concentration increases, the local relative growth rate flattens along the basal facet and, for Ga concentrations $\gtrsim 0.8$, exhibits a shallow double maximum at the boundary between the bottom and sidewalls (barely visible in the figure). This is not necessarily unexpected [31], and a refinement of the adatom kinetic parameters could clarify this behavior as it results from the interplay between diffusion and incorporation. This is a matter for future work.

To better visualize the segregation effects, Fig. 3(c) shows the enhancement of the relative Ga growth rate in the middle of the template compared to the nominal growth rate. This figure also shows the fit to experimental data in Ref. [32] for the Ga concentration of a pyramidal structure grown under similar conditions to those employed here, calculated from

$$x_{\mathrm{Ga}}^{\mathrm{eff}} = \frac{k(1-x)}{k(1-x)+x}, \tag{9}$$

for nominal Al content x with $k = 8.6$ a fitting parameter. Good agreement is obtained between this formula and our calculations (the small mismatch might be reduced with further optimization of our kinetic parameters), confirming that our model can predict the actual concentration of Ga incorporated along the vertical axis of the pyramid and is revealed, therefore, to be useful for designing structures requiring a specific alloy composition for a particular device application.

To investigate the temperature dependence of the self-limiting width, Eq. (8) was solved for $T = 830$–1000 K with a fixed Al concentration of 0.3. Figure 3(d) compares the calculated values of L_b^* with the experimental values extrapolated from cross-sectional AFM profiling measurements from the batch II. The model predicts, in near-perfect agreement with the experiments (parameter optimizations again might lead to a better agreement), a widening of the self-limiting width as the temperature increases, owing to the enhanced growth rate on the bottom of the template as a consequence of capillarity-driven

surface diffusion (which increases with the temperature) from the sidewalls toward the basal plane.

In summary, we have introduced a theoretical model which comprehensively reproduces the main experimentally observable phenomena during the growth by MOVPE of pyramidal QDs and VQWRs. The reaction-diffusion equations formulated here account for the interplay between precursor decomposition, adatom diffusion, and incorporation on the different crystallographic facets of the seeding template and can be extended to study the morphological evolution of any patterned surface. These results pave the way toward a reproducible on-demand design of seeded low-dimensional nanostructures and establish solid foundation for the future development of quantum-based technologies. Indeed, our improved understanding of the growth process has enabled us to obtain, for the first time, ordered arrays of entangled photon emitters, rather than isolated emitters, on a single wafer [33].

This research was enabled by the Irish Higher Education Authority Program for Research in Third Level Institutions (2007–2011) via the INSPIRE programme and by Science Foundation Ireland under Grants No. SFI/05/IN.1/I25 and No. SFI/10/IN.1/I3000. We are grateful to K. Thomas for his support with the MOVPE system.

[1] M. Ozdemir and A. Zangwill, J. Vac. Sci. Technol. A **10**, 684 (1992).
[2] E. Kapon, D. M. Hwang, and R. Bhat, Phys. Rev. Lett. **63**, 430 (1989).
[3] K. Dzurko, E. Menu, C. Beyler, J. Osinski, and P. Dapkus, Appl. Phys. Lett. **54**, 105 (1989).
[4] A. Madhukar, K. C. Rajkumar, and P. Chen, Appl. Phys. Lett. **62**, 1547 (1993).
[5] S. Koshiba, H. Noge, H. Akiyama, T. Inoshita, Y. Nakamura, A. Shimizu, Y. Nagamune, M. Tsuchiya, H. Kano, H. Sakaki, and K. Wada, Appl. Phys. Lett. **64**, 363 (1994).
[6] P. Atkinson, M. Ward, S. Bremner, D. Anderson, T. Farrow, G. Jones, A. Shields, and D. Ritchie, Physica (Amsterdam) **32E**, 21 (2006).
[7] S. Kiravittaya, A. Rastelli, and O. G. Schmidt, Appl. Phys. Lett. **88**, 043112 (2006).
[8] J. Skiba-Szymanska, A. Jamil, I. Farrer, M. B. Ward, C. A. Nicoll, D. J. P. Ellis, J. P. Griffiths, D. Anderson, G. A. C. Jones, D. A. Ritchie, and A. J. Shields, Nanotechnology **22**, 065302 (2011).
[9] A. Hartmann, L. Loubies, F. Reinhardt, A. Gustafsson, A. Sadeghi, and E. Kapon, Appl. Surf. Sci. **123–124**, 329 (1998).
[10] E. Kapon, G. Biasiol, D. M. Hwang, and E. Colas, Microelectron. J. **26**, 881 (1995).
[11] M. H. Baier, S. Watanabe, E. Pelucchi, and E. Kapon, Appl. Phys. Lett. **84**, 648 (2004).
[12] L. O. Mereni, V. Dimastrodonato, R. J. Young, and E. Pelucchi, Appl. Phys. Lett. **94**, 223121 (2009).
[13] A. Mohan, P. Gallo, M. Felici, B. Dwir, A. Rudra, J. Faist, and E. Kapon, Small **6**, 1268 (2010).
[14] P. Gallo, M. Felici, B. Dwir, K. A. Atlasov, K. F. Karlsson, A. Rudra, A. Mohan, G. Biasiol, L. Sorba, and E. Kapon, Appl. Phys. Lett. **92**, 263101 (2008).
[15] A. Mohan, M. Felici, P. Gallo, B. Dwir, A. Rudra, J. Faist, and E. Kapon, Nature Photon. **4**, 302 (2010).
[16] G. Bester, S. Nair, and A. Zunger, Phys. Rev. B **67**, 161306 (2003).
[17] M. A. Dupertuis, K. F. Karlsson, D. Y. Oberli, E. Pelucchi, A. Rudra, P. O. Holtz, and E. Kapon, Phys. Rev. Lett. **107**, 127403 (2011).
[18] A. L.-S. Chua, E. Pelucchi, A. Rudra, B. Dwir, E. Kapon, A. Zangwill, and D. D. Vvedensky, Appl. Phys. Lett. **92**, 013117 (2008).
[19] A. Dalla Volta, D. D. Vvedensky, N. Gogneau, E. Pelucchi, A. Rudra, B. Dwir, E. Kapon, and C. Ratsch, Appl. Phys. Lett. **88**, 203104 (2006).
[20] All samples were grown in a low-pressure horizontal reactor on substrates patterned by deep uv photolithography and wet chemical etching. The structure comprises a GaAs buffer and pairs of 120 nm $Al_xGa_{1-x}As$ and 15/25 nm GaAs markers grown at 0.5 ML/s with a V/III ratio $\sim$750.
[21] The AFM scans were acquired under atmospheric conditions immediately after cleaving the samples. Only samples for which the cleaving direction crosses the template in the proximity of the center, corresponding to the base of the profile, were selected. To avoid tip-resolution-related problems, tip shape characterization and image deconvolution processing were also carried out.
[22] I. Horcas, R. Fernandez, J. M. Gomez-Rodriguez, J. Colchero, J. Gomez-Herrero, and A. M. Baro, Rev. Sci. Instrum. **78**, 013705 (2007).
[23] E. Pelucchi, V. Dimastrodonato, A. Rudra, K. Leifer, E. Kapon, L. Bethke, P. A. Zestanakis, and D. D. Vvedensky, Phys. Rev. B **83**, 205409 (2011).
[24] P. Chen, J. Y. Kim, A. Madhukar, and N. M. Cho, J. Vac. Sci. Technol. B **4**, 890 (1986).
[25] T. Shitara, D. D. Vvedensky, M. R. Wilby, J. Zhang, J. H. Neave, and B. Joyce, Phys. Rev. B **46**, 6815 (1992).
[26] E. Pelucchi, S. Watanabe, K. Leifer, Z. Zhu, B. Dwir, P. De Los Rios, and E. Kapon, Nano Lett. **7**, 1282 (2007).
[27] A. Pimpinelli and J Villain, *Physics of Crystal Growth* (Cambridge University Press, Cambridge, 1998).
[28] J. Gravesen, M. Willatzen, and L. C. Lew Yan Voon, J. Math. Phys. (N.Y.) **46**, 012107 (2005).
[29] T. Takebe, M. Fujii, T. Yamamoto, K. Fujiita, and T. Watanabe, J. Appl. Phys. **81**, 7273 (1997).
[30] See Supplemental Material at http://link.aps.org/supplemental/10.1103/PhysRevLett.108.256102 for complementary geometry-related theoretical results.
[31] G. Biasiol, Ph.D. thesis, Swiss Federal Institute of Technology, 1998.
[32] Q. Zhu, E. Pelucchi, S. Dalessi, K. Leifer, M.-A. Dupertuis, and E. Kapon, Nano Lett. **6**, 1036 (2006).
[33] G. Juska, V. Dimastrodonato, L. O. Mereni, A. Gocalinska, and E. Pelucchi (unpublished).